A Simple Model of the Millimeter-Wave Scattering Parameters of Randomly Oriented Aggregates of Finite Cylindrical Ice Hydrometeors

J. A. WEINMAN

Atmospheric Sciences Department, University of Washington, Seattle, Washington

M.-J. KIM

Atmospheric Sciences Department, University of Washington, Seattle, Washington, and NASA Goddard Space Flight Center, Greenbelt, Maryland

(Manuscript received 18 September 2005, in final form 29 March 2006)

ABSTRACT

Spaceborne millimeter-wave radiometric measurements offer the potential to observe snowfall at high latitudes. A spaceborne W-band cloud radar on *CloudSat* has been able to observe snow. There is thus a need for a relatively simple representation of millimeter-wave scattering parameters of snow that can be incorporated into algorithms to retrieve snowfall from remotely sensed millimeter-wave brightness temperature measurements and for computing the millimeter-wave backscatter phase function of randomly oriented aggregates of ice prisms or columns.

The extinction coefficients, asymmetry factors, and backscatter phase functions describing scattering by randomly oriented aggregates of elongated cylinders were computed from the discrete dipole approximation. These parameters were also computed by means of a T-matrix model applied to single blunt cylinders by employing a phase delay that only depended on the frequency and the ratio of the volume to the projected area of the cylindrical aggregates. These scattering parameters were fitted by empirical analytical functions that only depended on that phase delay. This permitted consideration of numerous aggregate shapes with far less computational effort than that required by the discrete dipole approximation.

The results of this analysis were applied to measurements of millimeter-wave extinction, radar reflectivity, and snow size distributions obtained during the SNOW-TWO field experiment conducted by the U.S. Army in 1984. Although the simultaneity of the various measurements was not well documented, the theoretical results fell within the range of measurement uncertainty. Model results of the extinction coefficient and asymmetry factor needed to compute 183-GHz brightness temperatures measured by the NOAA Advanced Microwave Sounding Unit-B (AMSU-B) radiometers are presented in the appendix.

1. Introduction

The main component of the water cycle over mid-to-high latitudes is snowfall. Snowfall has been difficult to measure with snow gauges—especially when snowfall is light and drifting is significant. Even if adequate care is taken to measure snowfall, measurement sites are often sparse in remote high latitude or mountainous regions. Coverage by radar is also limited over these regions. This problem can be overcome to some extent by means of spaceborne millimeter-wave radiometric and radar measurements.

Microwave radiometers operating at frequencies where the atmosphere is relatively transparent have been available since 1978. It was difficult to measure snowfall from space because those radiometers operated at window frequencies less than 85 GHz where emission from the ground could confuse the analysis. The *NOAA-15*, *-16*, and *-17* satellites overcome some of the limitations encountered at lower frequencies. Those satellites carry Advanced Microwave Sounding Units-B (AMSU-B) that operate at 89 GHz, in the 150-GHz "dirty window" and in the 183-GHz water vapor absorption band (Saunders et al. 1994). Emission from partially snow-covered land surface is obscured by water vapor absorption in that band. Moreover the chan-

Corresponding author address: James A. Weinman, Atmospheric Sciences Department, University of Washington, Box 351640, Seattle, WA 98195-1640.
E-mail: Weinman@atmos.washington.edu

DOI: 10.1175/JAS3841.1

nels operating at frequencies greater than 85 GHz are more sensitive to scattering by snow so that it is possible to monitor snowfall within the atmosphere (Weng et al. 2003; Skofronick-Jackson et al. 2004; Kim 2004). The forthcoming Global Precipitation Mission (GPM) will include millimeter-wave radiometers to measure snowfall. Airborne radiometers have operated at frequencies even higher than 183 GHz.

The *CloudSat* satellite (Stephens et al. 2002) carries a W-band Cloud Profiling Radar that provides measurements of backscattering by snowfall. Millimeter-wave radars were used by Nemarich et al. (1988) and Wallace (1988) to measure the backscatter reflectivities at 96, 140, and 225 GHz. Photographic images of snow crystals were also obtained. The results of the present model are compared to those measurements.

Simplified representations of the scattering properties of randomly oriented irregularly shaped particles have been sought by treating those particles as equivalent spheres using Lorenz–Mie theory; see, for example, Takano and Liou (1989), Grenfell and Warren (1999), and Liu (2004). Unfortunately that approach has been hobbled because of the numerous criteria for defining the equivalent diameters, that is, equivalent volumes, surface areas, projected areas, ratios of volume to surface area, or spheres with diameters equal to the large dimension, but with reduced refractive indices. Infinite cylinders have also been used to represent such particles. A disadvantage of using spheres and infinite cylinders of nonabsorbing material with large refractive indices, such as those of ice at millimeter-wave frequencies, is that spurious partial wave resonances can be generated by those models. Those resonances are damped in the case of scattering by randomly oriented finite cylinders.

Although snow crystals are often in the form of hexagonal prisms, snow exhibits far more irregular morphology than such idealized prisms. It therefore suffices to compute the scattering properties of aggregates of cylinders. The T-matrix method (TMM) was used as a starting point to compute the extinction coefficients, asymmetry factors, and backscatter phase functions of single randomly oriented finite cylinders (Kim 2004). The TMM was introduced by Waterman (1971) and developed further by Barber and Yeh (1975) and Mishchenko and Travis (1998).

The scattering parameters of randomly oriented aggregates consisting of as many as four cylinders were derived from the discrete dipole approximation (DDA) described in Draine (1988). All of the DDA results could be approximated by the TMM model output for single finite cylinders by introducing an effective dimension, Δ, into a phase delay, ρ, cited by van de Hulst (1957).

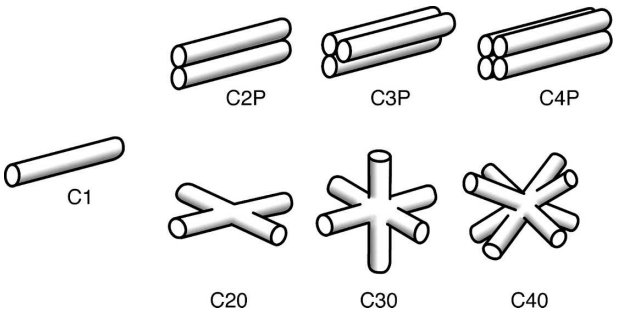

FIG. 1. Model crystal habits. From left to right, shapes are identified as C1 single cylinder, C2P two parallel cylinders, C2O two orthogonal cylinders, C3P three parallel cylinders, C3O three orthogonal cylinders, C4P four parallel cylinders, and C4O four nearly orthogonal cylinders.

2. Method

Because of the variegated shapes and orientations of snowflakes, calculation of their millimeter-wave scattering properties is a daunting effort. Nonetheless Kim (2004) computed the scattering properties of several idealized shapes of frozen hydrometeors, such as those shown in Fig. 1, using the DDA. The DDA algorithm provided by Draine and Flatau (2004) had numerous features to enhance computational efficiency; but it was still very time consuming when various sizes, habits, orientation angles, and frequencies were considered. Kim applied the DDA to computations at five frequencies between 95 and 340 GHz, to depict scattering from the seven particle shapes shown in Fig. 1. Fourteen large dimensions, which ranged between 0.06 and 3 mm, were modeled and the computations were conducted for 108 incident angles. (Scattered radiation was computed at six zenith angles between 0° and 90° and for six azimuth angles between 0° and 180°.) The aspect ratios, defined as the ratio of the diameter to the length of the constituent cylinders, were equal or greater than 0.24 for most of the computations. This required a total of 30 240 separate DDA computations. Although Kim found that the extinction coefficients and asymmetry factors were complicated functions of the orientation of the particles, their shapes and sizes, and the frequencies of the incident radiation, the scattering characteristics became greatly simplified for randomly oriented particles.

Shapes and refractive index of model frozen hydrometeors

We will consider the habit models shown in the idealized renditions of Fig. 1. These included single finite

cylinders (C1) and concatenations of two (C2P), three (C3P), and four (C4P) parallel cylinders and two (C2O), three (C3O), and four (C4O) orthogonal cylinders. These configurations approximate the possible extreme orientations of constituent cylinders within aggregates. Most aggregates may be expected to be configured between these extremes.

The model shapes are characterized by small, S, and large, L, dimensions; S is the diameter of the cylindrical constituents and L is their length. The small dimension $S = \alpha L$, where the aspect ratios are $\alpha = 0.1$, 0.24, 0.4, and 0.6. The first and second values, which are in the range of the findings of Hobbs et al. (1974) and Auer and Veal (1970), were used in the DDA computations while the third and fourth values were used in the TMM C1 computations. Most, but not all, cases considered in this study were restricted to $\alpha \geq 0.24$ because the computation times encountered in the DDA for small α became excessive. The TMM encountered computational difficulties when $\alpha < 0.3$ in accord with the findings of Kuik et al. (1994).

Bullets and blunt rosettes can be described with $\alpha > 0.3$. However, needles, of the type measured by Auer and Veal (1970), have $\alpha = 0.20L^{-0.59}$ for $L > 1$ mm. The multiple cylinders comprising the aggregates, CN . . . , used in this study have the same S–L relationships as C1. Although we confined our study to limited values of α, those can be rescaled to account for other values of α, L, and N. The density δ is set to 0.91 g cm^{-3} and the refractive index, $m = m' - jm'' = 1.78 - j\,0.004$ in accord with Mätzler and Wegmüller (1987).

3. Phase delay parameter

The phase delay is $\rho = 2\pi\Delta(m - 1)\nu/c$ from van de Hulst (1957), where ν is the frequency and c is the speed of light.

a. Randomly oriented single finite cylinder

The effective dimension, Δ, that is used to compute the phase delay of cylinders can be generalized to

$$\Delta = 4V(N, L)/\pi A_{\perp}(N, L), \tag{1a}$$

where N is the number of cylinders in the aggregate. For a single infinite cylinder, $V(1, L)$ is the volume; that is, $\pi\alpha^2L^3/4$, and $A_{\perp}(1, L)$ is the area projected perpendicular to the direction of the incident radiation; that is, αL^2, so that $\Delta = S$, the diameter of an infinite cylinder.

Stephens (1984) showed that for oblique incidence on an infinitely long cylinder, $\Delta = S/\sin(\theta_1)$, where θ_1 is the angle between the cylinder axis and the propagation direction. For a randomly oriented cylinder, $\sin(\theta_1)$ weighted over all solid angles is

$$\langle \sin(\theta_1) \rangle = 2\pi \int_0^{\pi} \sin^2(\theta_1)\, d\theta_1/4\pi = \pi/4. \tag{1b}$$

The end surfaces of finite cylinders are oriented perpendicularly to the cylinder axis at an angle θ_1' with respect to the direction of the incident propagation so that $\sin(\theta_1')$ weighted over all solid angles is

$$\langle \sin(\theta_1') \rangle = 2\pi \int_0^{\pi} \sin(\theta_1 + \pi/2) \sin(\theta_1)\, d\theta_1/4\pi = \tfrac{1}{2}. \tag{1c}$$

It follows that the projected area of a single randomly oriented finite cylinder is

$$A_{\perp}(1, L) = \langle \sin(\theta_1) \rangle \alpha L^2 + \langle \sin(\theta_1') \rangle \pi(\alpha L/2)^2, \tag{2a}$$

where the first right-hand term represents the projection of the side of the cylinder and the second right-hand term represents the projection of the exposed end surface. Applying the results of Eqs. (1b) and (1c) to (1a) and (2a) yields

$$\Delta = 4\alpha L/\pi(1 + \alpha/2), \tag{2b}$$

for C1.

b. Randomly oriented aggregation of parallel cylinders

Reasoning similar to that employed for a single cylinder can be used to derive an effective dimension, Δ, for aggregates of N parallel cylinders, (P). Cylinders, in CNP configurations, can obscure each other so that the projected area, $A_{\perp}^{\mathrm{P}}(N, L)$, for such aggregates is considerably less than that of equal number of exposed orthogonal cylinders. This obscuration depends upon the rotation angle, φ, of the aggregate around the axis of symmetry. The projected area can be averaged over φ to yield

$$A_{\perp}^{\mathrm{P}}(2, L) = \{[(1 + \tfrac{1}{2})\alpha L^2]\langle \sin(\theta_2) \rangle + [2\pi(\alpha L/2)^2]\langle \sin(\theta_2') \rangle\} \tag{3a1}$$

for two parallel cylinders, C2P. The first term on the right-hand side is the mean of the area of the perpendicular projection and that which occurs when one cylinder completely obscures the other. Similarly,

$$A_{\perp}^{\mathrm{P}}(3, L) = \{[(1 + \tfrac{1}{2} + \sqrt{3}/4)\alpha L^2]\langle \sin(\theta_3) \rangle + [3\pi(\alpha L/2)^2]\langle \sin(\theta_3') \rangle\} \tag{3a2}$$

for three parallel cylinders, C3P, and

$$A_{\perp}^{\mathrm{P}}(4, L) = \{[(1 + \tfrac{1}{2} + 1/\sqrt{2})\alpha L^2]\langle\sin(\theta_4)\rangle + [4\pi(\alpha L/2)^2]\langle\sin(\theta_4')\rangle\} \quad (3a3)$$

for four parallel cylinders, C4P. Here again the first right-hand term is the mean of the perpendicular projection and that obtained when one or two cylinders partially obscure the other one or two at 60° and 45°, respectively. The second right-hand terms are projections of the cylinder end surfaces.

The volume is linearly proportional to the number of cylinders, so it follows that

$$\Delta = 4\alpha L/\pi(\gamma_N + \alpha/2), \quad (3b)$$

according to Eq. (1a). Simple geometry yields $\gamma_2 = 0.75$, $\gamma_3 = 0.5 + \sqrt{3}/12 = 0.64$, and $\gamma_4 = 0.375 + 0.25/\sqrt{2} = 0.55$ for C2P, C3P, and C4P, respectively.

c. *Randomly oriented aggregation of orthogonal cylinders*

The effective dimension, Δ, for an aggregation of N orthogonal (O) cylinders differs from that of parallel cylinders with the same volume because their projected areas will be greater than those for N parallel cylinders. Some additional factors must be considered: The effective lengths of all additional cylinders are reduced by $(1 - \alpha)$ to account for the overlap with the first cylinder. The volume, $V(N, L)$, of the N orthogonal cylinders in the aggregate is

$$V(N, L) = \pi\alpha^2 L^3[1 + (N - 1)(1 - \alpha)]/4. \quad (4)$$

Here, $A_{\perp}^{\mathrm{O}}(N, L)$ is the area projected perpendicular to the incident radiation that can be derived from the probability that radiation is not intercepted by a cylinder. The ratio of the projected area intercepted by the first cylinder in Eq. (2a) to that of a disc that encloses the cylinder defines the probability that radiation is intercepted, namely,

$$\Pi(1) = \alpha(1 + \alpha/2), \quad (5a)$$

and the probability, $P(1)$, that radiation is not intercepted is just $1 - \Pi(1)$.

The remaining $N - 1$ finite cylinders are oriented perpendicular to the first cylinder axis at an angle θ_N with respect to the direction of the incident propagation

$$\tan(\theta_N) = -\cot(\theta)/\cos(\varphi), \quad (5b)$$

where φ is the azimuth angle around the axis of the first cylinder. The sine of that projected angle weighted over the entire solid angle is

$$\langle\sin(\theta_N)\rangle = 2/\pi \int_0^{\pi/2}\int_0^{\pi/2} \frac{\cos(\theta)\sin(\theta)\, d\theta\, d\varphi}{\sqrt{\cos^2(\theta) + \sin^2(\theta)\cos^2(\varphi)}} = 2/\pi. \quad (5c)$$

The probability, $\Pi(N)$, that radiation is intercepted by any of the $N - 1$ cylinders that are orthogonal to the first cylinders is

$$\Pi(N) = \{[(1 - \alpha)\alpha L^2]\langle\sin(\theta_N)\rangle + [\pi(\alpha L/2)^2]\langle\sin(\theta_N')\rangle\}/(\pi L^2/4). \quad (5d)$$

The first right-hand term in the square bracket is the area of the cylinder side. Note that the length of each cylinder is reduced by a factor of $(1 - \alpha)$ because each of the $(N - 1)$ cylinders intersects the first cylinder thereby removing αL from the projected length. The first right-hand square bracket is weighted by $\langle\sin(\theta_N)\rangle$ to account for the projection of that surface in the direction of the incident radiation. The second right-hand term in the square bracket is the area of the cylindrical end surface and it is weighted by $\langle\sin(\theta_N')\rangle = \pi/4$ to account for the projection of that surface in the direction of the incident radiation. The denominator is just the area of the disc that encloses the aggregate.

If the aggregate contains N cylinders, then the probability that radiation is not intercepted by those cylinders is

$$P(N) = [1 - \Pi(1)][1 - \Pi(N)]^{N-1}, \quad (6a)$$

so that the probability of interception by an aggregation of N cylinders is $1 - P(N)$ and that determines the projected area by

$$A_{\perp}^{\mathrm{O}}(N, L) = [1 - P(N)]\pi L^2/4. \quad (6b)$$

4. Extinction coefficients, asymmetry factors, and backscatter phase functions

The extinction cross section, C_{ext} (mm^2), generally increases with the size of the hydrometeor. This dynamic range can be reduced by considering the extinction cross section per unit mass, M (mg),

$$C_{\mathrm{ext}}/M = Q(\rho)A_{\perp}^{i}(N, L)/\delta V(N, L). \quad (7a)$$

Here, $Q(\rho)$ is the extinction efficiency, and i is an index that identifies parallel (P), orthogonal (O) or the mean (M) morphology of the aggregate. We can thus define the dimensionless

$$Q(\rho)/\rho = [c\delta/8(m - 1)]C_{\mathrm{ext}}/(M\nu). \quad (7b)$$

The asymmetry factor, g, is

$$g = 2\pi \int_0^{\pi} \cos(\Theta) \sin(\Theta)[P(\Theta)/4\pi]\, d\Theta, \tag{8}$$

where $P(\Theta)$ is the phase function of the scattering angle, Θ.

Thomas and Stamnes (1999, p. 213) showed that phase functions could be approximated by a merged Rayleigh–Henyey–Greenstein function:

$$P(\Theta)/4\pi = \frac{3(1 - g^2)[1 + \cos(\Theta)^2]}{8\pi(2 + g^2)[1 + g^2 - 2g\cos(\Theta)]^{3/2}}. \tag{9}$$

This approximation becomes a monotonically decreasing function of the scattering angle, Θ, as $g > 0$. It cannot represent a glory. This one-parameter representation can be used to compute the radar reflectivity from the asymmetry factor:

$$\eta = C_{\text{ext}} P(180°). \tag{10}$$

5. Results

Figure 2 shows that $Q(\rho)/\rho$ depends only upon ρ irrespective of the orientation of the cylinders comprising the aggregates (O or P). Computation of $Q(\rho)/\rho$ for single randomly oriented finite cylinders were readily implemented with the TMM because it is much faster than the DDA. Unfortunately the TMM does not yield trustworthy results for values of $\alpha < 0.3$. All other data points were derived from the DDA applied to single cylinders and aggregates consisting of up to four cylinders. Those cylinders were characterized mainly by $\alpha = 0.24$ and a few cases with $\alpha = 0.1$. The results appear to be nearly invariant for all aggregates up to $\rho < 3.5$. This finding is consistent with that which Baran (2003) found for infrared scattering by cirrus aggregates. It is thus only necessary to compute $Q(\rho)/\rho$ for randomly oriented finite cylinders with a single α, say $\alpha = 0.4$, by means of the TMM formalism to derive $Q(\rho)/\rho$ as a function of ρ that is applicable to a broad range of parameters. The quantity $C_{\text{ext}}/(M\nu)$ can then be scaled for aggregates at various frequencies, ν, for differing habits (O or P) and with different aspect ratios, α, provided that the particle size and frequency preserve $\rho < 3.5$, or even 5 depending on the desired accuracy. This constraint may create problems for C4P aggregates with $L \sim 4$ mm at frequencies greater than 200 GHz where $\rho > 5$.

Because radiative transfer models needed to retrieve snowfall from millimeter-wave measurements may require simple parameterizations of $C_{\text{ext}}/(M\nu)$, we empirically fitted an analytic approximation to the data shown in Fig. 2. Thus,

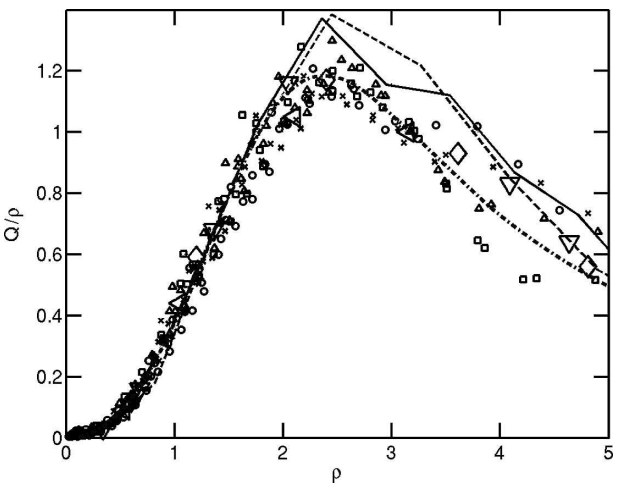

FIG. 2. The extinction efficiency, Q, divided by the phase delay, $\rho = 2\pi\Delta(m - 1)\nu/c$. The points for C1 (○), C2O (×), C3P (◊), C3O(△), C4P (▽), and for C4O (□) are for $\alpha = 0.24$ and $0.20L^{-0.59}$ using the DDA, from Kim (2004). The large symbols are P cases and the small symbols are O cases. The TMM results for C1 are for $\alpha = 0.4$ (solid line)and $\alpha = 0.6$ (dashed line). The empirical function in Eq. (11a) is represented by the dashed–dotted line. Note that the data were obtained at various frequencies, $95 < \nu < 340$ GHz, over sizes $0.06 < L < 3$ mm.

$$Q(\rho)/\rho = 0.40\rho^{2.1}/(1 + 0.031\rho^{4.1}). \tag{11a}$$

The behavior of Eq. (11a) for small ρ is consistent with the finding of van de Hulst (1957, p. 316), who showed that $Q \sim (r\nu)^3$ for thin needles with radius, r. No physical significance appears to be attached to any of the other numbers that occur in Eq. (11a).

Figure 3 shows that the asymmetry factor scales consistently with ρ as well. It approaches a limiting value of 0.76 for large values of ρ in accord with the formalism developed by Irvine (1963). The formalism for that limiting value was developed for large spheres, but the result depended only on the refractive index of the sphere, it thus should be applicable to particles of any shape. Figure 3 (right) appears to bear that out.

Because it is also desirable to have a simple function to represent g, an empirical fit to data presented in Fig. 3 is

$$g = 0.30\rho^{2.1}/(1 + 0.18\rho^{2.6}). \tag{11b}$$

No physical significance appears to be attached to this function either; it is merely convenient.

The normalized backscatter phase function can be computed from g by Eq. (9):

$$P(180°)/4\pi = 3(1 - g)/4\pi(2 + g^2)(1 + g)^2. \tag{11c}$$

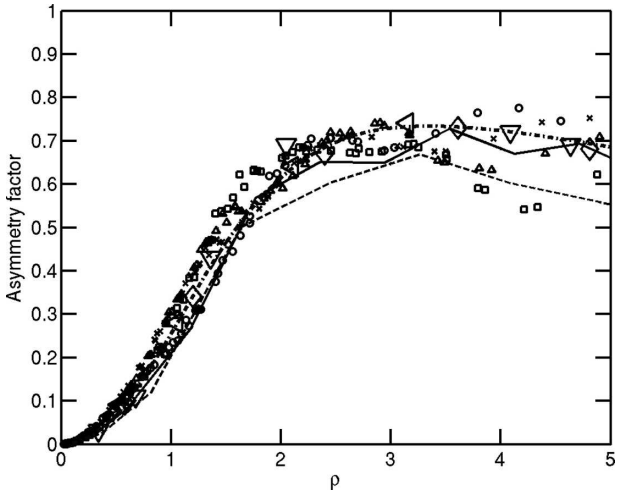

FIG. 3. Asymmetry factor, g, as a function of ρ for aggregates of cylinders. The empirical function in Eq. (11b) is represented by the dashed–dotted line. Other symbols are the same as those in Fig. 2.

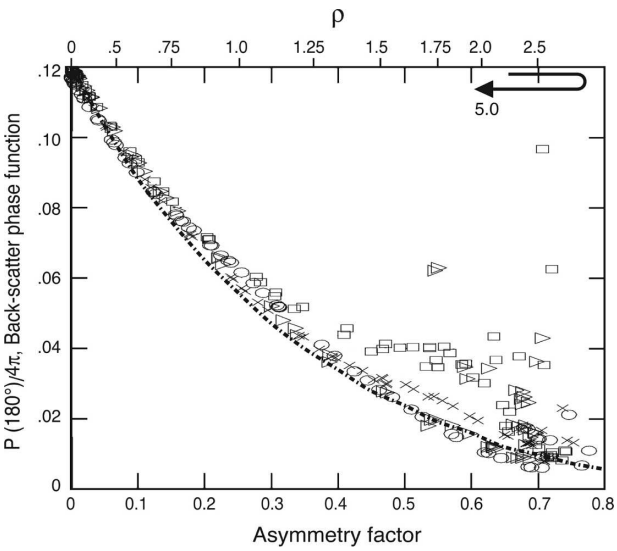

FIG. 4. The normalized backscatter phase function, $P(180°)/4\pi$, as a function of the asymmetry factor, g. The points are for C1, (○), C2O (×), C3O(△), and for C4O (□). The dashed–dotted curve represents Eq. (11c). Phase delays, ρ, presented on the scale above the figure are those associated with the asymmetry factors displayed on the lower scale. Because Eq. (11b) is not a single-valued function, the ρ scale curves back on itself for $\rho > 3.3$.

The normalized backscatter phase function is shown in Fig. 4 as a function of g where it is compared to the results of the DDA computations. Corresponding values of ρ are also shown on the uppermost axis.

The DDA results were well represented by Eq. (11c) for $g < 0.4$ ($\rho < 1.5$) for all of the configurations and for the C1, C2O, C2P configurations for $g < 0.7$ ($\rho < 5$). Some, but not all, of the DDA computations for C3O, C3P, C4O, and C4P exhibited enhanced backscattering that departed significantly from Eq. (11c) for $1.5 < \rho < 5$. Although it is unlikely that this is a glory caused by interference between surface waves and forward diffracted waves, as in the case of scattering by spheres, the effect may still be real. Videen et al. (1998) showed that interference effects for scattering from aggregated spheres produced enhanced backscatter when the separation between two spheres was less than a wavelength. On the other hand the enhanced backscatter may be a numerical artifact caused by considering too few orientation angles or too few dipoles in the DDA computations. We could not pursue this problem in more depth because the DDA computations became prohibitively time consuming for those cases.

6. A comparison with attenuation and backscatter phase function measurements

a. Extinction coefficient per unit mass

The mass, M (mg), of snow as a function of its dimension, L (mm), can be written as $M = \zeta L^{\xi}$. Locatelli and Hobbs (1974) found $\zeta = 0.037$ and $\xi = 1.9$, Holroyd (1987) found $\zeta = 0.0085$ and $\xi = 2.1$, and Mitchell et al. (1990) found $\zeta = 0.089$ and $\xi = 2.0$. Auer and Veal (1970) found that $S = 0.20L^{0.41}$ for $L > 1$ mm, which yields $\alpha = 0.20L^{-0.59}$. Using this α–L relationship produces $\zeta = (0.026 \pm 0.001)N^{0.93\pm0.02}$ and $\xi = 1.88 \pm 0.03$, for $1 \leq N \leq 3$.

A field experiment, designated SNOW-TWO, was conducted by the U.S. Army Cold Regions Research and Engineering Laboratory (CRREL) during the winter of 1983/84 (Nemarich et al. 1988; Wallace 1988; Jordan 1984). Backscatter and attenuation at millimeter-wave frequencies and particle size distributions were among the diverse measurements obtained during SNOW-TWO. Images of snow prisms, such as that depicted in Fig. 5 (upper), were recorded during SNOW-TWO: "With the camera directed perpendicularly to the plane of the glass slides, the areas of the snow crystal images displayed on the monitor were measured. To develop size distributions, each area measurement was converted to a projected diameter, i.e., the diameter of a circle of equal area" (Jordan 1984). We thus can define the effective diameter as

$$D_{\text{eff}} = \sqrt{4A_{\perp}/\pi}. \tag{12}$$

No information was available regarding the number of needles that contributed to D_{eff} and whether that number varied with D_{eff} for the case depicted in Fig. 5.

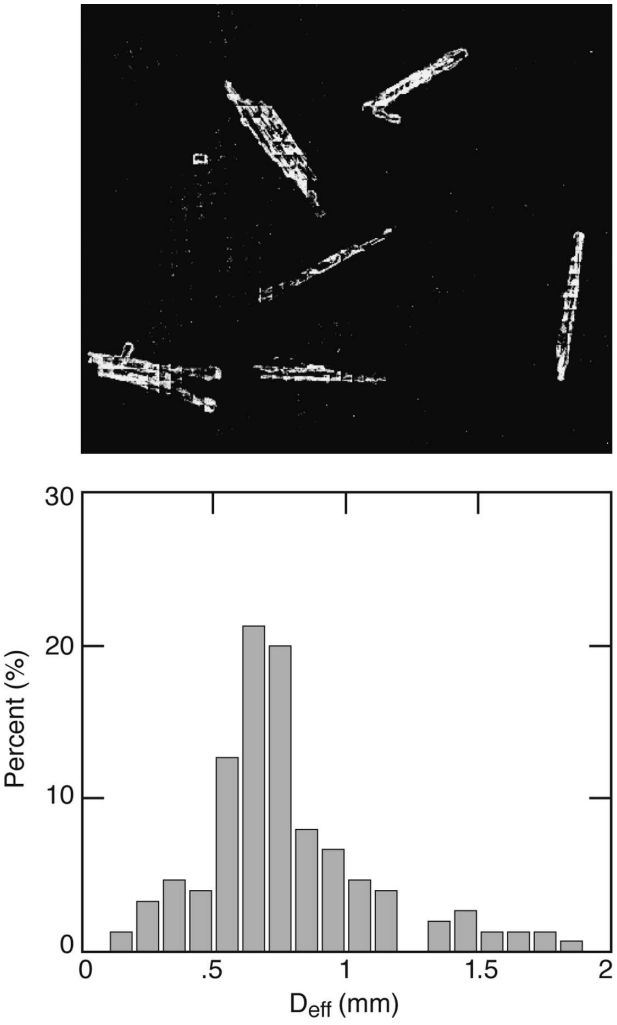

FIG. 5. (upper) Example of snow crystal observations at 1700 local time (LT) 23 Jan 1984 near the ground during the SNOW-TWO field experiment. (lower) Size distribution as a function of D_{eff}. Distribution of D_{eff} (mm) was measured from samples such as that shown above. The mode occurs at $D_{\text{eff}} = 0.8 \pm 0.2$ mm. From Jordan (1984).

While one could compute the scattering parameters of an ensemble of aggregates with the size distribution shown in Fig. 5 (lower), it may suffice to consider particles with a mode value of $D_{\text{eff}} \sim 0.8 \pm 0.2$ mm because of that ambiguity.

Table 1 presents values of D_{eff} derived from orthogonal, $A_{\perp}^{\text{O}}(N, L)$; parallel, $A_{\perp}^{\text{P}}(N, L)$; and their mean values $A_{\perp}^{\text{M}}(N, L) = \frac{1}{2}[A_{\perp}^{\text{O}}(N, L) + A_{\perp}^{\text{P}}(N, L)]$ of the projected area computed for aggregates of cylinders. Those cylinders have aspect ratios that depend on L as cited by Auer and Veal. The italicized entries in Table 1 are those that produce, $D_{\text{eff}} = 0.8 \pm 0.2$ mm. The results for cylinders with $N = 1$ and $L = 2$ mm and those with $N = 2$ and $L = 2$ mm, irrespective of whether they are orthogonal or parallel, fall within the measured range of D_{eff} that was most prevalent. [Other configurations can fall within this range, but only with more restrictions; i.e., either $A_{\perp}^{\text{O}}(N, L)$ or $A_{\perp}^{\text{P}}(N, L)$ do not satisfy that constraint.]

The attenuation coefficients,

$$A^{i}(N, L) = 10 \log_{10}(C_{\text{ext}}/M) \text{ dB km}^{-1} (\text{g m}^{-3})^{-1}, \tag{13}$$

were computed from Eqs. (7b) and (11a) for C1, C2P, C2O, and C2M, where superscript i can be O, P, or M. Figure 6 presents $A^{i}(N, L)$ as a function of frequency for those configurations with $L = 2$ mm. The phase delay, ρ, is less than 4 even at $\nu = 300$ GHz, so that Eq. (11a) is applicable. Those computations are compared to measurements obtained at 35, 96, 140, and 225 GHz during SNOW-TWO. It is noteworthy that the double value of C_{ext}/M causes the C2P curve to diminish as the frequency increases beyond 150 GHz so that the growth of $A^{\text{M}}(2, 2)$ with frequency is slowed. Care should be taken in applying the present model if $N > 2$, $L > 2$ mm, and for frequencies $\nu > 150$ GHz to assure that $\rho < 5$. This condition can be easily violated by parallel cylinders. Fortunately, they are an extreme idealization.

b. Backscatter phase function

Radar reflectivities for 96, 140, and 225 GHz were also measured during the SNOW-TWO experiment. Table 2 presents a comparison between the normalized backscatter phase function for the C1, C2O, C2P, and C2M configurations derived for $L = 2$ mm from Eq. (11c). These values are compared to measurements described by Nemarich et al. (1988), Wallace (1988), and

TABLE 1. The effective diameter, D_{eff} (mm), from Eq. (12) for $\alpha = 0.20L^{-0.59}$ for orthogonal (O) and parallel (P) cylinders and for the mean (M) from Eqs. (3a) and (6b). Roman font entries have D_{eff} that fall outside the range of 0.8 ± 0.2 mm. Bold entries fall within this range, but only italicized bold entries have all shapes within this range.

L (mm), α	C1	C2O	C2P	C2M	C3O	C3P	C3M	C4O	C4P	C4M
1, 0.200	0.47	0.59	0.41	0.50	**0.67**	0.39	0.53	**0.73**	0.36	0.55
2, 0.133	***0.75***	***0.97***	***0.66***	***0.81***	1.12	0.61	**0.87**	1.25	0.57	**0.91**
3, 0.104	***1.00***	1.29	**0.87**	1.08	1.51	**0.81**	1.16	1.69	**0.75**	1.22
4, 0.088	1.21	1.58	1.06	1.32	1.86	**0.99**	1.42	2.09	**0.92**	1.50

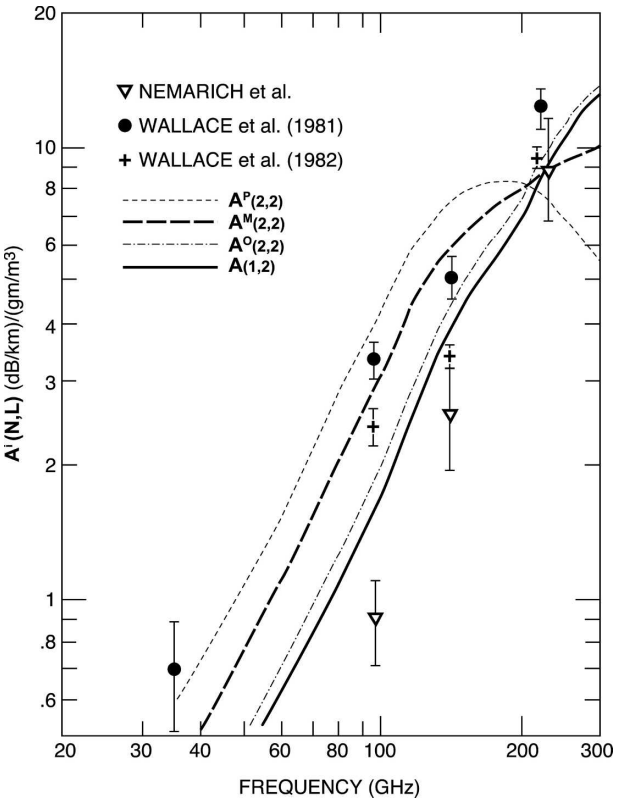

FIG. 6. Attenuation, $A^i(N, L)$, computed from this model for $N = 1$ and 2 for $L = 2$ mm and $i =$ O, P, and M. Results are for cylinders configured as C1, C2P, C2O, and C2M. Data were measured by Nemarich et al. (1988) and Wallace (1988).

Jordan (1984). Although Table 1 shows that the C1, C2O, C2P, and C2M can account for the measured $A^i(N, L)$, the model backscatter phase function for C2M, shown in boldface type in Table 2, yields the best agreement with the measurements. The 96-GHz model results are in some disagreement with the measurements; however, the 96-GHz measurements have greater uncertainty than those at the higher frequencies. The remaining computations fall within the measured uncertainties. It should be noted that SNOW-TWO was not conducted to validate millimeter-wave scattering models; a more focused experiment would be desirable.

7. Discussion and conclusions

There have been numerous attempts to represent the scattering parameters of aggregates of cylinders by equivalent spheres. However scaling the diameters to suitable geometric features of those shapes has been a vexing task, Mishchenko et al. (2002). The present formalism derives the scattering parameters of randomly oriented aggregates of finite cylinders by employing the TMM for single finite cylinders, but with suitably scaled phase delays. Although aspect ratios, $\alpha < 0.3$, were difficult to compute with the TMM, the DDA results suggest that scaling the ρ parameter in the manner described in this analysis allows the TMM results to be extended to smaller aspect ratios.

Simple analytical functions were empirically fitted to the data provided by the TMM and DDA. These may be useful for applications that require rapidly evaluated representations of C_{ext}/M, g and $P(180°)/4\pi$.

In this study we compared the scattering parameters of aggregates consisting of up to four cylinders oriented either orthogonally or parallel to each other. The C_{ext}/M and g results were in reasonable agreement for $\rho < 3.5$. Fortunately that encompasses cylindrical aggregates that are up to ~3 mm long at frequencies <200 GHz. The solutions diverged more for $3.5 < \rho < 5.0$ but they may still be useful for some radiative transfer models.

The normalized backscattering phase functions were well behaved for $\rho < 1.5$ for all of the configurations that were considered. Enhanced backscattering phase functions were encountered for C3O and some C4O cases, but all others were well behaved up to $\rho \leq 5.0$. We could not determine the validity of the computed enhanced backscattering phase functions. However it is gratifying that all orthogonally configured aggregates

TABLE 2. The backscatter phase functions at $\nu = 96$, 140, and 225 GHz from Eq. (11c) for C1, C2O, C2P, and C2M aggregates with $L = 2$ mm and Auer and Veal's α compared to measurements obtained during SNOW-TWO. The bold entries are model results that are most consistent with the measurements.

	ν = 96 GHz			ν = 140 GHz			ν = 225 GHz		
	ρ	g	$P(180°)/4\pi$	ρ	g	$P(180°)/4\pi$	ρ	g	$P(180°)/4\pi$
C1	0.50	0.068	0.097	0.73	0.142	0.078	1.17	0.327	0.043
C2O	0.56	0.086	0.092	0.82	0.178	0.070	1.32	0.390	0.035
C2P	1.30	0.384	0.036	1.90	0.590	0.016	3.05	0.731	0.008
C2M	0.93	0.226	**0.060**	1.36	0.409	**0.033**	2.19	0.653	**0.012**
$P(180°)/4\pi$ measurement		0.024 ± 0.018			0.031 ± 0.009			0.017 ± 0.009	

with $L \leq 4$ mm, and even aggregates containing less than three constituent cylinders with $L \leq 2$ mm in a parallel configuration, yield $\rho < 1.5$ at 95 GHz. Thus one may expect the results of this study to be applicable to snow retrievals from *CloudSat* radar measurements.

Numerous measurements of snow particle mass, M, as a function of the large dimension, L, of the particles suggest that $M \sim L^2$. Results of the limited measurements of C_{ext}/M by Nemarich et al. (1988), Wallace (1988), and Jordan (1984) suggest that a model employing one or two cylinders with a length of ~2 mm and a morphology that lies between the O and P configurations could account for both the $M - L$ and the C_{ext}/M measurements. The particles shown in Fig. 5 (upper) appear to be similar to those modeled cylindrical aggregates. The aspect ratio of the displayed prisms is $\alpha \sim 0.1$, a value that is consistent with the $\alpha \sim 0.133$ cited in the left-hand column of Table 1 that was based on the measurements of Auer and Veal (1970). The few aggregates shown in this figure appear to contain no more than two particles, consistent with the model. Although this is encouraging, other habits may also satisfy these conditions. Unfortunately the sample displayed by Jordan (1984), shown in Fig. 5 (upper), was small.

The phase delay, ρ, was introduced in van de Hulst's (1957) anomalous diffraction theory (ADT). ADT requires that the effective dimension, Δ, of the scattering particle to be larger than the wavelength of the incident radiation. ADT also neglects reflection from the surface of the scattering particle and refraction within the particle. The premise that $|m - 1| \ll 1$ allows this neglect. Although this condition was not met by the present case ($m = 1.78$), van de Hulst (1957, p. 177) found that the extinction coefficient for scattering by a sphere could be derived from ADT even when $m = 2.0$.

Applying the TMM to cylinders with an effective diameter defined in terms of the ratio of volume to projected area enabled Baran (2003) to derive similar parameters of cirrus particle aggregates at infrared wavelengths. While the aggregate dimensions and wavelengths differ, the underlying physics is comparable. Baran noted that the sharp edges of finite cylinders were significant. Liu et al. (1998) computed the scattering properties of randomly oriented finite cylinders. Their study found that difference between ADT and TMM results diminished with nonsphericity thereby demonstrating the importance of the cylindrical end surfaces. Spheres and infinite cylinders with large real indices of refraction are high-Q resonators for some partial waves so that resonances may be encountered. It appears that the effect of end surfaces on finite cylinders reduces the Q of those resonators thereby damping those partial waves and leaving the interference term between the diffracted and transmitted radiation as the dominant component of the observed scattering.

The projected area, $A^i_\perp(N, L)$, was found to be a critical factor in this study. This is demonstrated in Fig. 6 where C_{ext}/M can differ by as much as ~2 for particles with nearly the same N and L; that is, particles with equal volumes but differing $A^i_\perp(N, L)$. This suggests that the millimeter-wave scattering properties of snow aggregates need to be measured along with 2D optical imagery that determines the projected area, $A^i_\perp(N, L)$. The volume, $V(N, L)$, can be determined by melting the aggregate and recording images of the drops. A field experiment to measure the snow shapes and sizes along with the millimeter-wave scattering characteristics of various snow habits and snowfall rates is strongly encouraged. The SNOW-TWO field experiment may provide guidance for planning.

Any polydisperse snow particle size distribution will diffuse the results of this study. It should be stressed that the idealized models depicted in Fig. 1 are probably not the only habits that can be fitted to the various measurements that may be encountered. However, a mixture of these idealized aggregates may be adequate for use in snowfall retrievals if no other information is available.

Acknowledgments. We wish to thank Dr. Bruce Draine for his helpful comments that enabled us to activate the DDA program. We also wish to thank Ms. Beth Tully for her graphic work on this paper. This study was supported by NASA Grant NCC-5-584, S-69019-G, and NAG5-9668. We also wish to thank Dr. Gail Skofronick-Jackson and Dr. Ramesh Kakar for their encouragement and interest in this work. An unidentified reviewer encouraged us to amplify several points that were insufficiently addressed in the first draft of this manuscript. We are grateful for that guidance.

APPENDIX

Properties of Cylindrical Ice Aggregates with Size-Dependent Aspect Ratios at 183 GHz

Because of their widespread availability, the most likely application of this study will be the analysis of data from the AMSU-B sensors. We present tabulations of ρ, of the extinction per unit mass, C_{ext}/M, and asymmetry factors, g, that are usually employed in such analyses at $\nu = 183$ GHz, the water vapor absorption line measured by AMSU-B. The aspect ratio, α, is chosen to depend on the cylinder length as cited by Auer and Veal (1970).

TABLE A1. The phase delay, ρ, at $\nu = 183$ GHz for $\alpha = 0.20L^{-0.59}$ for orthogonal (O) and parallel (P) cylinders and for the mean (M). The italic values may be suspect because $\rho > 5$.

L (mm), α	C1	C2O	C2P	C2M	C3O	C3P	C3M	C4O	C4P	C4M
1, 0.200	0.69	0.79	1.79	1.29	0.88	3.07	1.97	0.96	4.67	2.81
2, 0.133	0.95	1.07	2.48	1.78	1.16	4.27	2.72	1.24	*6.54*	3.89
3, 0.104	1.14	1.28	2.98	2.13	1.37	*5.15*	3.26	1.45	*7.91*	4.68
4, 0.088	1.29	1.45	3.38	2.42	1.54	*5.86*	3.70	1.62	*9.02*	*5.32*

TABLE A2. Extinction cross section (mm^2) per mass (mg), C_{ext}/M, at $\nu = 183$ GHz for $\alpha = 0.20L^{-0.59}$ for orthogonal (O) and parallel (P) cylinders and for the mean (M) from Eq. (10a) and Table 1. The italic entries with $\rho > 5$ may be suspect.

L (mm), α	C1	C2O	C2P	2M	C3O	C3P	C3M	C4O	C4P	C4M
1, 0.200	0.98	1.12	2.09	1.60	1.23	1.44	1.34	1.34	0.53	0.94
2, 0.133	1.33	1.49	1.91	1.70	1.59	0.68	1.14	1.69	*0.20*	0.94
3, 0.104	1.56	1.72	1.52	1.62	1.82	*0.40*	1.11	1.89	*0.11*	1.00
4, 0.088	1.73	1.88	1.19	1.54	1.96	*0.28*	1.12	2.01	*0.07*	*1.04*

TABLE A3. Asymmetry factor, g, at $\nu = 183$ GHz for $\alpha = 0.20L^{-0.59}$ for orthogonal (O) and parallel (P) cylinders from Eq. (10b) and Table 1. The italic entries with $\rho > 5$ may be suspect.

L (mm), α	C1	C2O	C2P	C2M	C3O	C3P	C3M	C4O	C4P	C4M
1, 0.200	0.11	0.15	0.50	0.32	0.17	0.71	0.44	0.20	0.72	0.46
2, 0.133	0.20	0.25	0.65	0.45	0.28	0.73	0.50	0.31	*0.66*	0.48
3, 0.104	0.27	0.32	0.71	0.51	0.36	*0.70*	0.53	0.39	*0.61*	0.50
4, 0.088	0.33	0.39	0.72	0.56	0.42	*0.68*	0.55	0.45	*0.58*	*0.51*

Table A1 presents examples of values of ρ as a function of the lengths, L, of aggregates of N cylinders. Results for orthogonal, parallel cylinders and the mean values are shown. Table A2 shows the corresponding extinction cross section per mass, C_{ext}/M ($mm^2\ mg^{-1}$), derived from Eq. (11a) and Table A3 shows the corresponding asymmetry factor, g, derived from Eq. (11b). The present analysis was confined to $\rho \leq 5$. The lightly shaded values may be suspect because $\rho > 5$ for those cases.

REFERENCES

Auer, A. H., and D. L. Veal, 1970: The dimension of ice crystals in natural clouds. *J. Atmos. Sci.,* **27,** 919–926.

Baran, A. J., 2003: Simulation of infrared scattering from ice aggregates by use of a size shape distribution of circular ice cylinders. *Appl. Opt.,* **42,** 2811–2818.

Barber, P. W., and C. Yeh, 1975: Scattering of electromagnetic waves by arbitrarily shaped electric bodies. *Appl. Opt.,* **14,** 2864–2872.

Draine, B. T., 1988: The discrete dipole approximation and its application to interstellar graphite grains. *Astrophys. J.,* **333,** 848–872.

——, and P. J. Flatau, 2004: User guide for the discrete dipole approximation code, DDSCAT.6.0. [Available online at http://arxiv.org/abs/astro-ph/0409262v2.]

Grenfell, T. C., and S. G. Warren, 1999: Representation of a nonspherical ice particle by a collection of independent spheres for scattering and absorption of radiation. *J. Geophys. Res.,* **104,** 31 697–31 709.

Hobbs, P. V., S. Chang, and J. D. Locatelli, 1974: The dimensions and aggregation of ice crystals in natural clouds. *J. Geophys. Res.,* **79,** 2199–2206.

Holroyd, E. W., 1987: Some techniques and uses of 2D-C habit classifications software for snow particles. *J. Atmos. Oceanic Technol.,* **4,** 498–511.

Irvine, W. M., 1963: The asymmetry of the scattering diagram of a spherical particle. *Bull. Astron. Neth.,* **17,** 176–184.

Jordan, R., Ed., 1984: Snow-two data report. Vol. 2. U.S. Army Cold Regions Research & Engineering Laboratory, Special Rep. 84-20, 179–219.

Kim, M.-J., 2004: A physical model to estimate snowfall over land using microwave measurements. Ph.D. thesis, University of Washington, 151 pp.

Kuik, F. J., J. F. de Haan, and J. W. Hovenier, 1994: Single scattering of light by circular cylinders. *Appl. Opt.,* **33,** 4906–4918.

Liu, G., 2004: Approximation of single scattering properties of ice and snow particles for high microwave frequencies. *J. Atmos. Sci.,* **61,** 2441–2456.

Liu, Y., W. P. Arnott, and J. Hallett, 1998: Anomalous diffraction theory for arbitrarily oriented finite circular cylinders and comparison with exact T-matrix results. *Appl. Opt.,* **37,** 5019–5030.

Locatelli, J. D., and P. V. Hobbs, 1974: Fall speeds and masses of solid precipitation particles. *J. Geophys. Res.,* **79,** 2185–2198.

Mätzler, C., and U. Wegmüller, 1987: Dielectric properties of

fresh-water ice at microwave frequencies. *J. Phys. D.,* **20,** 1623–1630.

Mishchenko, M. I., and L. D. Travis, 1998: Capabilities and limitations of a current FORTRAN implementation of the T-matrix method for randomly oriented, rotationally symmetric scatterers. *J. Quant. Spectrosc. Radiat. Transfer,* **60,** 309–324.

——, J. Hovenier, and L. Travis, 2002: *Scattering, Absorption and Emission of Light by Small Particles.* Cambridge University Press, 439 pp.

Mitchell, D. L., R. Zhang, and R. Pitter, 1990: Mass-dimensional relationship for ice particles and the influence of riming on snowfall rates. *J. Appl. Meteor.,* **29,** 153–163.

Nemarich, J., J. Wellman, and J. Lacombe, 1988: Backscatter and attenuation by falling snow and rain at 96, 140 and 225 GHz. *IEEE Trans. Geosci. Remote Sens.,* **26,** 319–329.

Saunders, R. W., S. J. English, and D. C. Jones, 1994: AMSU-B: A new tool for atmospheric research. *Proc. SPIE,* **2313,** 98–107.

Skofronick-Jackson, G. M., M. J. Kim, J. A. Weinman, and D.-E. Chang, 2004: A physical model to determine snowfall over land by microwave radiometry. *IEEE Trans. Geosci. Remote Sens.,* **42,** 1047–1058.

Stephens, G. L., 1984: Scattering of plane waves by soft obstacles: Anomalous diffraction theory for circular cylinders. *Appl. Opt.,* **23,** 954–959.

——, and Coauthors, 2002: The CloudSat mission and the A-Train: A new dimension of space-based observations of clouds and precipitation. *Bull. Amer. Meteor. Soc.,* **83,** 1771–1790.

Takano, Y., and K. N. Liou, 1989: Solar radiative transfer in cirrus clouds. Part I: Single scattering and optical properties of hexagonal ice crystals. *J. Atmos. Sci.,* **46,** 3–19.

Thomas, G. E., and K. Stamnes, 1999: *Radiative Transfer in the Atmosphere and Ocean*. Cambridge University Press, 213 pp.

van de Hulst, H. C., 1957: *Light Scattering by Small Particles*. J. Wiley & Sons, 470 pp.

Videen, G., R. G. Pinnick, D. Ngo, Q. Fu, and P. Chylek, 1998: Asymmetry parameter and aggregate particles. *Appl. Opt.,* **37,** 1104–1109.

Wallace, H. B., 1988: Millimeter-wave propagation measurements at the Ballistic Research Laboratory. *IEEE Trans. Geosci. Remote Sens.,* **26,** 253–258.

Waterman, P. C., 1971: Symmetry, unitarity and geometry in electromagnetic scattering. *Phys. Rev. D,* **3,** 825–839.

Weng, F., L. Zhao, R. R. Ferraro, G. Poe, O. Li, and N. C. Grody, 2003: Advanced microwave sounding unit cloud and precipitation algorithm. *Radio Sci.,* **38,** 8086–8096.